

Ore genesis of Badi copper deposit, northwest Yunnan Province, China: evidence from geology, fluid inclusions, and sulfur, hydrogen and oxygen isotopes

Hejun Yin¹ · Jianguo Huang¹ · Tao Ren¹

Received: 8 August 2017 / Revised: 12 October 2017 / Accepted: 13 November 2017 / Published online: 25 November 2017
© Science Press, Institute of Geochemistry, CAS and Springer-Verlag GmbH Germany, part of Springer Nature 2017

Abstract The Badi copper deposit is located in Shangjiang town, Shangri-La County, Yunnan Province. Tectonically, it belongs to the Sanjiang Block. Vapor–liquid two-phase fluid inclusions, CO₂-bearing fluid inclusions, and daughter-bearing inclusions were identified in sulfide-rich quartz veins. Microthermometric and Raman spectroscopy studies revealed their types of ore-forming fluids: (1) low-temperature, low-salinity fluid; (2) medium-temperature, low salinity CO₂-bearing; and (3) high-temperature, Fe-rich, high sulfur fugacity. The $\delta^{18}\text{O}$ values of chalcopyrite-bearing quartz ranged from 4.96‰ to 5.86‰, with an average of 5.40‰. The δD values of ore-forming fluid in equilibrium with the sulfide-bearing quartz were from – 87‰ to – 107‰, with an average of – 97.86‰. These isotopic features indicate that the ore-forming fluid is a mixing fluid between magmatic fluid and meteoric water. The $\delta^{34}\text{S}$ values of chalcopyrite ranged from 13.3‰ to 15.5‰, with an average of 14.3‰. Sulfur isotope values suggest that the sulfur in the deposit most likely derived from seawater. Various fluid inclusions coexisted in the samples; similar homogenization temperature to different phases suggests that the Badi fluid inclusions might have been captured under a boiling system. Fluid boiling caused by fault activity could be the main reason for the mineral precipitation in the Badi deposit.

Keywords Badi copper deposit · Fluid inclusion · Sulfur isotope · Hydrogen and oxygen isotope · Ore genesis

1 Introduction

The Sanjiang metallogenic belt is located in the eastern part of the Tethys tectonic domain. The belt underwent tectonic evolution during the Late Paleozoic to Mesozoic Tethys subduction orogeny and the Cenozoic collision orogeny (Wang et al. 2009; Liu 1983; Xu et al. 2012, 2015). The Sanjiang metallogenic belt includes four secondary metallogenic belts: the Dege-Xiangcheng Cu–Pb–Zn–Ag metallogenic belt (DXMB), the Jinsha River–Ailaoshan Au–Cu–Pt metallogenic belt (JAMB), the Jomda–Weixi–Lüchun Fe–Cu–Pb–Zn metallogenic belt (JWMB), and the Changdu–Lanping–Puer Cu–Pb–Zn–Ag metallogenic belt (CLMB). DXMB includes the Zhuoma and Lannitang epithermal copper polymetallic deposit (Liu et al. 2016; Gou et al. 2010), the Pulang and Xuejiping porphyry copper deposit (Li et al. 2011; Leng et al. 2012), and the Hongshan and Langdu skarn copper deposit (Zu et al. 2015; Jin et al. 2013). In JAMB, the representative deposits include the Donggualin gold deposit, the Yangla copper deposit, and the Sanjiacun Pb–Zn deposit (Pan et al. 2000). The Laojunshan VHMS massive sulfide Pb–Zn deposit and Zuna SEDEX Ag–Pb–Zn deposit (Feng et al. 2011) are the representative deposits in JWMB. CLMB includes the Yulong and Narigongma porphyry copper deposit and the Jinding Pb–Zn deposit (Tang et al. 2006). The Badi copper deposit belongs to JAMB. The deposit is a recent prospecting discovery. No relevant article has yet been published about the Badi deposit, and ore-forming conditions, ore-controlling factors, and precipitation mechanisms are still unknown. In this paper, we use fluid

✉ Jianguo Huang
460880511@qq.com

Tao Ren
rtao1982@126.com

¹ Kunming University of Science and Technology,
Kunming 650093, China

inclusion microthermometric data and Raman spectroscopy, as well as sulfur, oxygen, and hydrogen isotope compositions to constrain the origin, nature, and evolution of ore-forming fluids and then discuss ore-forming mechanisms and ore genesis.

1.1 Geologic setting

The Badi copper deposit is located east of the Jinsha River, in southeast of Shangri-La County, Yunnan Province (Fig. 1a). Tectonically, it is situated in the Qinghai-Tibet-Yunnan sub block (Hu et al. 2005; Shao 1989). The Shigu

metamorphic belt is exposed in the Jinsha River geosyncline fold (Ren 1980) and includes the Proterozoic Shigu group and Cambrian to Triassic strata. The Shigu metamorphic belt is connected with the Diancangshan metamorphic rocks in Eryuan County. The belt is bounded by the Jinsha River fault to the west and Shigu-Judian fault to the east. The Paleozoic rocks belong to platform-type clastic, carbonate, and basic volcanic rocks, and the rock sequence is similar to the stratigraphic units of the Yangtze Platform. Therefore, it is generally believed that Shigu metamorphic rock is a part of the crystalline basement of the Yangtze Block (Zhai et al. 1993). The Shigu Group,

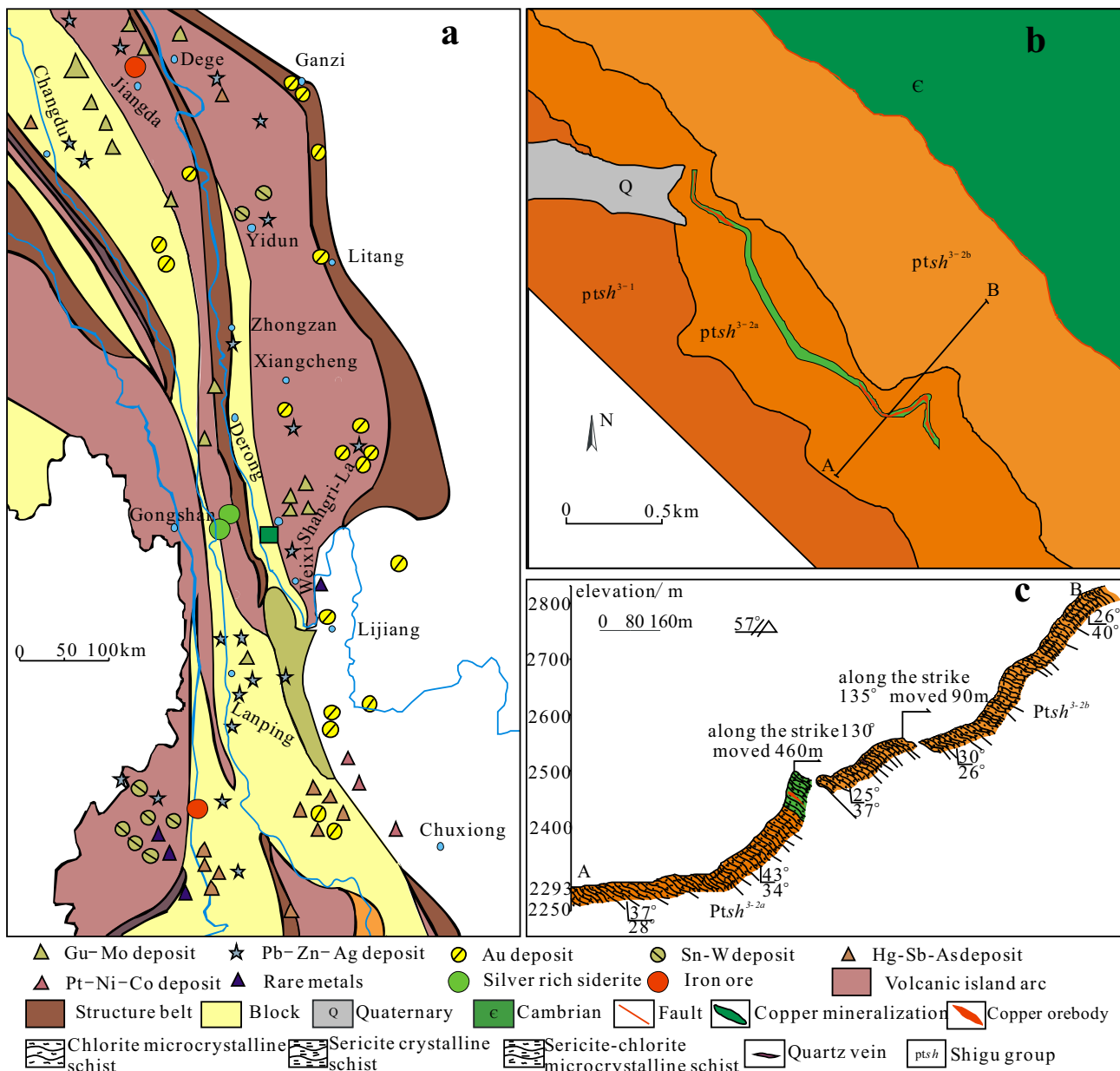
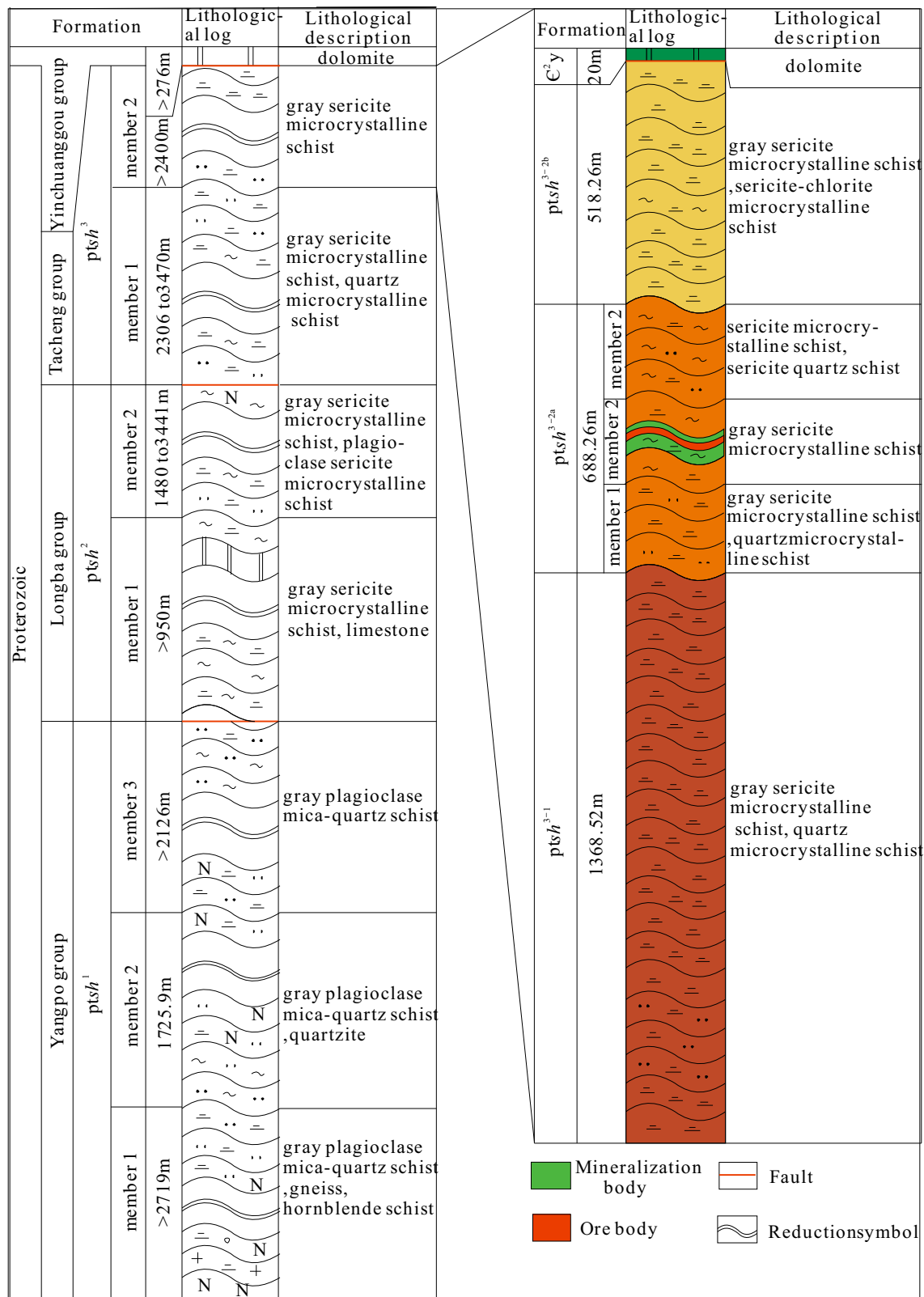


Fig. 1 **a** Regional geological map of the Badi region (after Li et al. 2013); **b** geological map of the Badi copper deposit; **c** the measured geological profile in the Badi mine

**Fig. 2** The stratigraphic column figure of the Badi deposit

with a thickness of about 10,000 meters, can be divided into the Yangpo, Longba, and Tacheng Formations from bottom to top (Fig. 2). According to the plagioclase-amphibolite Sm–Nd isochrone age of 1369.8 to 1343.8 Ma, predecessors determined the Yangpo Formation is Paleoproterozoic (Li 2003; Zhai et al. 1990).

1.2 Geology of the Badi deposit

The strata exposed in the Badi deposit are predominantly upper Proterozoic Shigu Group and can be divided into three sets: Ptsh³⁻¹, Ptsh^{3-2a}, and Ptsh^{3-2b} (Cui et al. 2014). Ptsh³⁻¹ consists mainly of grayish green to dark gray sericite microcrystalline schist, sericite microcrystalline quartz schist, and sericite phyllite. According to mineral and lithological characteristics, Ptsh^{3-2a} (Fig. 1b, c) can be subdivided into three members from bottom to top: a gray to dark sericite microcrystalline schist and quartz microcrystalline schist, with occasional meta-basic rock and quartz lens; the main ore host strata of gray to green sericite quartzite microcrystalline schist, with a partial basalt mezzanine, and with several 0.7 to 8 m layers containing copper-bearing quartz veins; and a dark sericite microcrystalline schist and sericite quartz schist. At the top of Ptsh³⁻², copper-bearing quartz occurring as lenses has thickness of 0.79 to 1.97 m. Ptsh^{3-2b} consists of gray to grayish green quartz microcrystalline schist. The Upper Cambrian Yinchuanggou Formation consists of a medium thickness of light to gray pyrite-bearing dolomite. Due to metamorphism, the strata display various scales of fold structures (Fig. 3b–d). The arc-shaped Shigu-Qizong fault passes through the east side of the mine.

The ore bodies in the Badi copper deposit are mainly hosted in the sericite quartz microcrystalline schist. The near-ore wall rocks are mostly chlorite and silicates, with sulfide-bearing quartz veins. In the mine, one copper mineralization belt (Fig. 1b) was found along a NW–SE trend, with a length of more than 3000 m, width of 50 to 80 m, and a maximum thickness of 100 m. In the southeast and northwest sections of the belt, a number of industrial ore bodies have been delineated. The ore bodies have complex shapes and various thicknesses. V₁ ore body, located between prospecting lines 0 and 1, presents lenticular bedding with the stratum (Fig. 1c). The ore body is 100 m long, with thickness of 3 to 5 m. Copper grades vary from 0.12% to 5%, with an average of 3.14%. Copper metal reserve is more than 30,000 t.

According to mineral assemblage, the ore in the mine was divided into two types: (1) Sericite-sulfide type: mainly composed of chalcopyrite, sericite, chlorite, quartz, and cordierite. The metamorphic mineral assemblage is sericite + chlorite + quartz, which belongs to low green schist facies. A large number of lenticular and gut-shaped

quartz and chlorite veins run through the schist; spotty chlorite was also observed in the quartz veins. Chalcopyrite occurs as disseminated veinlets in the quartz veins or along the contact zone between coarse quartz veins and sericitites. Little massive chalcopyrite co-exists with pyrite (Fig. 3e, f, l). Pyrite occurs as idiomorphic or hypidiomorphic granular crystals. This mineral assemblage contains a lot of malachite (Fig. 3a, e, f), which is the secondary copper mineral in the ore. (2) Quartz-sulfide type: the main ore type in the deposit. Mineral association is sericite + quartz, with quartz occurring as veins, lenses (Fig. 3d, g, i). The quartz measured in width 2 to 3 m and 10 to 15 m in length. Disseminated, veinlet, and locally spotted chalcopyrite was observed in quartz veins. According to the sequence of mineral precipitation, we present a mineral paragenetic sequence for the Badi copper deposit (Table 1).

2 Sampling and analytical methods

The samples for fluid inclusion microthermometric study are sulfide-rich quartz veins from drill core between prospecting lines 0 and 1. More than 20 doubly polished thin sections were prepared for optical observation; 12 representative samples were chosen for laser Raman spectroscopic and microthermometric analyses. Microthermometric measurements were carried out using a Linkam THMS600 heating-freezing stage with a temperature range from –195 to +600 °C at the State Key Laboratory for Mineral Deposit Research, Nanjing University. The accuracy of the measured temperatures was approximately ±0.2 °C during both cooling and heating from 100 to 600 °C. The salinities of NaCl–H₂O inclusions were calculated using the final melting temperatures of ice (Lu et al. 2004; Bodnar 1993; Liu and Shen 1999; Davis et al. 1990); those of CO₂-bearing fluid inclusions were calculated using the melting temperatures of clathrate (Collins 1979; Bodnar 1989). The compositions of single fluid inclusions were identified by a Renishaw RM2000 Raman microprobe equipped with an Ar ion laser with a surface power of 5 mW for exciting the radiation (514.5 nm).

The samples for sulfur isotope analyses were taken from both surface exposures and a drill core in the Badi deposit. Five samples (LB81 to LF003) were separated from quartz-sulfide type ore; others were separated from sericite-sulfide type ore. Sulfide grains were carefully hand-picked under a binocular microscope after the samples had been crushed, cleaned, and sieved to 40 to 60 mesh, resulting in a separate of 99% pure sulfides, using a Finnigan MAT251EM mass spectrometer at the Analytical Laboratory of the Beijing Research Institute of Uranium Geology. Sulfur isotope ratios are reported as δ³⁴S relative to the Canyon Diablo

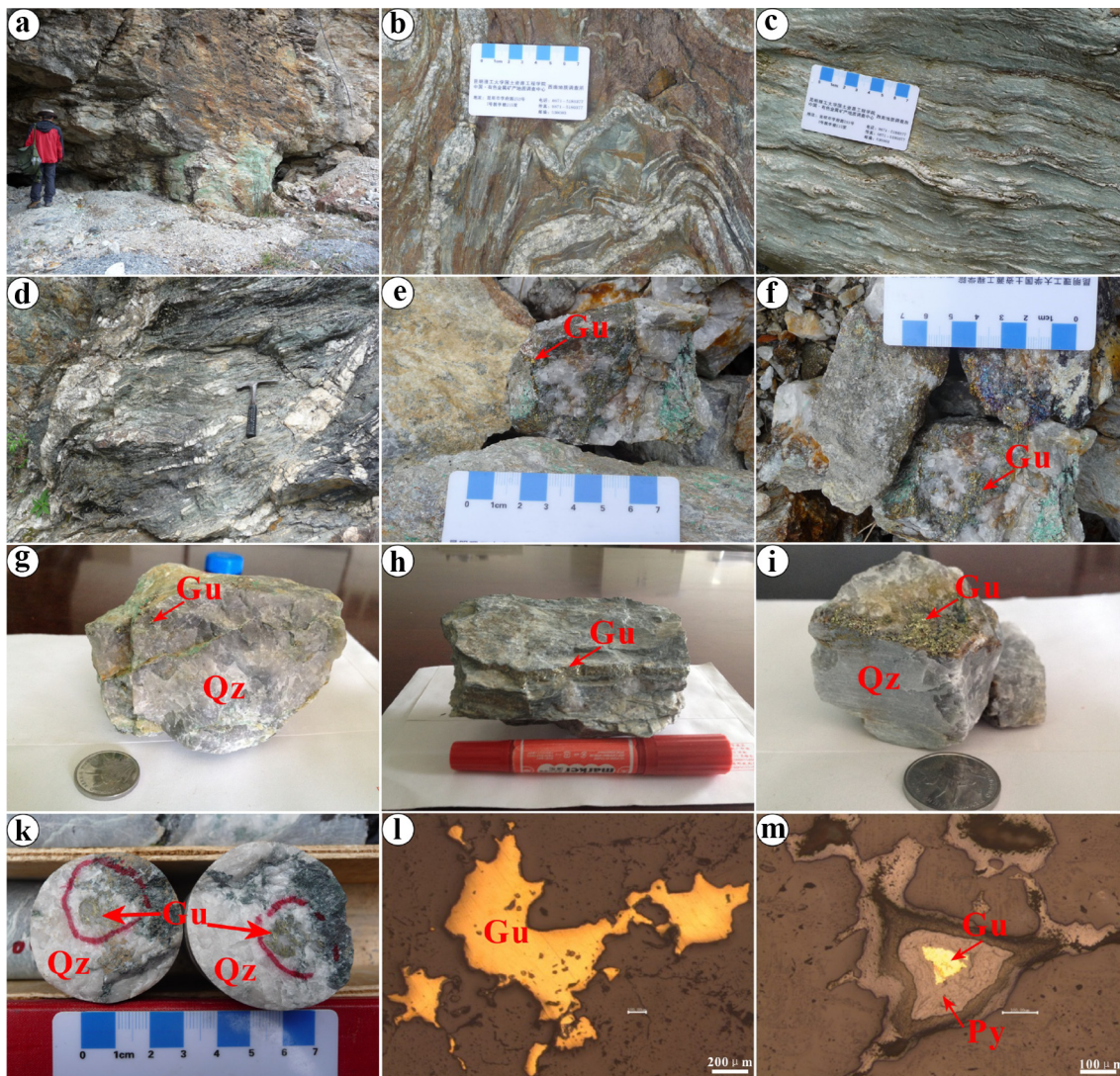


Fig. 3 **a** Malachite in the mine; **b, c** small folds of the Badi deposit; **d** interbedded quartz vein; **e, f**, disseminated chalcopyrite texture and malachite aggregation; **g** disseminated chalcopyrite in the quartz vein; **h** the pyrite veins in the schist; **i** film-like chalcopyrite on the quartz surface; **j** spotted chalcopyrite in drilling core; **k, l** chalcopyrite, pyrite under the microscope

Troilite (CDT). Precision for sulfur isotopic analysis was better than $\pm 0.2\text{\textperthousand}$; specific methods for sulfur isotope analysis followed the description by Liu et al. (2013).

Five samples of quartz-sulfide type ore (LB018 to LB022) and two samples of sericite-sulfide type ore were prepared for hydrogen and oxygen isotope analysis. Oxygen isotopic compositions of the quartz, and hydrogen isotopic compositions of water in fluid inclusions of quartz were determined using a MAT 253EM mass spectrometer at the Analytical Laboratory of the Beijing Research Institute of Uranium Geology. Oxygen gas was generated from the samples by quantitative reaction with BrF_5 in externally heated nickel vessels. Hydrogen in the extracted water from the fluid inclusions within quartz separates was replaced by zinc at about 600 °C and released for mass

spectrometry. The $\delta^{18}\text{O}$ values of quartz and δD values of water were reported relative to Vienna standard mean ocean water (V-SMOW); analytical precision was better than $\pm 0.2\text{\textperthousand}$ for $\delta^{18}\text{O}$ values of quartz, and $\pm 2\text{\textperthousand}$ for δD values of water. Detailed analytical procedures followed those described by Liu et al. (2013).

3 Analytical results

3.1 Fluid inclusion petrography and microthermometry

Samples collected from sulfide-bearing quartz veins were used for fluid inclusion study. According to the phase types

Table 1 Mineral paragenetic sequence in Badi copper deposit

Mineral Mineralization stage \ Mineral	Early ore forming stage	Main ore forming stage	Late ore forming stage	Supergene stage
Quartz	—	—	—	—
Sericite	—	—	—	—
Chlorite	—	—	—	—
Cordierite	—	—	—	—
Pyrite	—	—	—	—
Chalcopyrite	—	—	—	—
Malachite	—	—	—	—
Covellite	—	—	—	—

and filling characteristics of the fluid inclusions at room temperature and the phase transition in the cooling process, the fluid inclusions can be divided into the following types:

I-type vapor–liquid two-phase fluid inclusions This type is most abundant in ore-bearing quartz veins. These fluid inclusions occur as clusters or isolated, with diverse shapes, generally from 5 to 10 µm in size. According to the liquid/vapor phase volume ratios, they were further divided into two subtypes.

Ia-type liquid-rich fluid inclusions (Fig. 4a) are usually isolated or clustered. Few co-exist with II-type fluid inclusions. Homogenization temperatures were from 116.4 to 322.0 °C, mainly concentrated in range of 163.1 to 214.3 °C. Ice-melting temperatures were – 10.7 to – 0.20 °C (Fig. 6), with corresponding salinities from 0.35 wt% to 14.67 wt% NaCl equivalent (Fig. 7).

Ib-type vapor-rich fluid inclusions (Fig. 4b) These are rare; only three fluid inclusions of this type were found. At room temperature, vapor and liquid phases existed. Their shapes are flat oval, with vapor/liquid volume ratios at or above 2:1, and size of 5 to 10 µm. These inclusions were observed to coexist with Ia-type inclusions. At temperatures of 193 to 457 °C (Fig. 5), they homogenized to one phase. Ice-melting temperatures were – 6.9 to – 4.8 °C (Fig. 6); calculated salinities ranged from 7.59 wt% to 10.35 wt% NaCl equivalent (Fig. 7). One fluid inclusion homogenized to the vapor phase, with a higher homogenization temperature. The other two inclusions

homogenized to the liquid phase, with a lower homogenization temperature.

II-type CO₂-bearing fluid inclusions According to the phase at room temperature, these were further divided into two subtypes:

IIa-type CO₂-bearing two-phase inclusions (Fig. 4c) These inclusions were two-phase at room temperature, mostly present as flat ovals, 5 to 15 µm. Vapor/liquid ratios were greater than 2:1. When cooling to about – 0.4 °C, these fluid inclusions formed new bubbles in the CO₂ phase and the original V_{CO₂} changed to L_{CO₂} + V_{CO₂}. At the same time, the inclusions transformed from two-phase (L_{H₂O} + V_{CO₂}) to three-phase (L_{H₂O} + L_{CO₂} + V_{CO₂}). Their homogenization temperatures were 211.7 to 269.0 °C (Fig. 5), with salinities of 0.53 to 0.71 wt% NaCl equivalent (Fig. 7).

IIb-type CO₂-rich three-phase inclusions (L_{H₂O} + L_{CO₂} + V_{CO₂}) (Fig. 3d) presented three phases at room temperature. All of these inclusions were independent in sulfide quartz, with a size of 5 to 10 µm. Eutectic temperatures were between – 59.3 and – 56.7 °C, indicating the existence of vapor content other than CO₂.

Temperatures of CO₂ clathrate samples varied from 3.0 to 8.4 °C (n = 10), mainly concentrated at 5.0 to 8.0 °C; corresponding salinities varied from 3.15 wt% to 11.89 wt% NaCl equivalent (Fig. 7), concentrated at 3.15 wt% to 4.62 wt% NaCl equivalent. There were two methods of homogenization for IIb-type fluid inclusions:

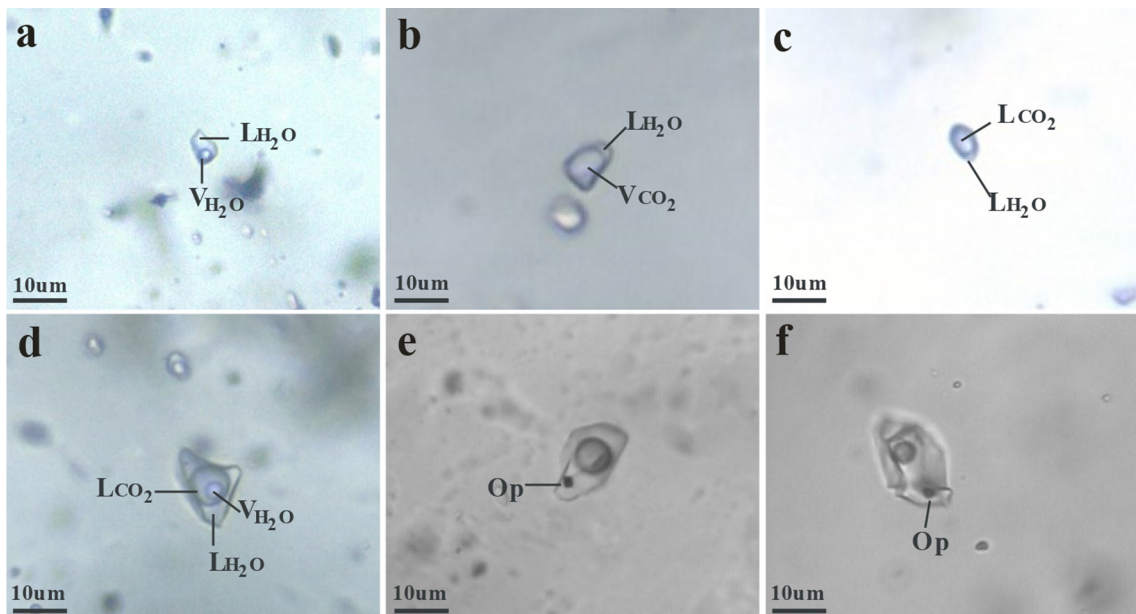


Fig. 4 **a** Liquid-rich fluid inclusions; **b** vapor-rich fluid inclusions; **c** inclusions with a single CO_2 bubble at room temperature and an aqueous phase; **d** inclusions with CO_2 liquid and vapor phase; **e** fluid inclusions contain one pyrite daughter mineral; **f** speculate that the daughter mineral is chalcopyrite; Op: opaque daughter mineral

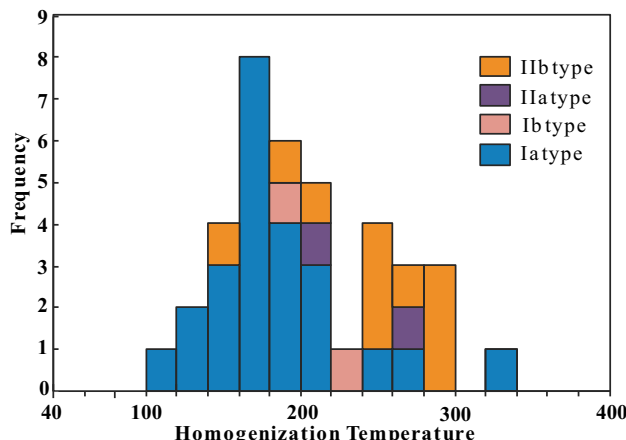


Fig. 5 Frequency histogram of total homogenization temperatures ($^{\circ}\text{C}$; burst temperature is excluded)

(1) homogenization to the vapor phase; partial homogenization temperatures were 18.7 to 25.8 $^{\circ}\text{C}$ and (2) homogenization to the liquid phase; partial homogenization temperatures were 21.5 to 30.4 $^{\circ}\text{C}$. These inclusions had a final homogenization temperature range of 156.6 to 296.3 $^{\circ}\text{C}$, concentrated at 193.4 to 296.3 $^{\circ}\text{C}$ (Table 2).

III-type daughter mineral-bearing fluid inclusions (Fig. 4e, f) had vapor, liquid, and solid phases and generally irregular morphology, with a size of 5 to 20 μm . Daughter minerals in these inclusion samples were all opaque, and cubic or triangular. The ice melt temperatures were -9.7 to -2.8 $^{\circ}\text{C}$ (Fig. 6), with salinity of 4.55

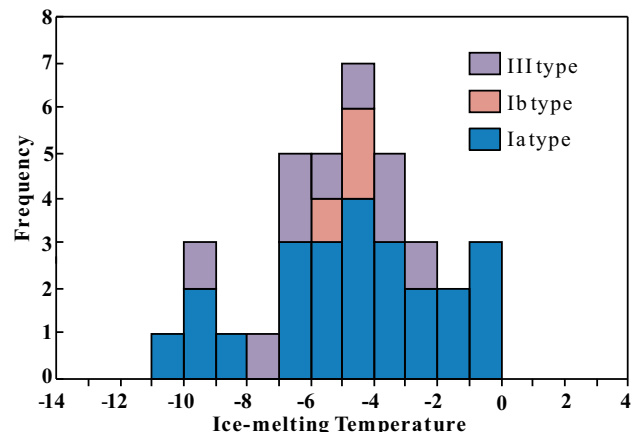


Fig. 6 Frequency histogram of ice-melting temperature ($^{\circ}\text{C}$)

wt% to 13.62 wt% NaCl equivalent (Fig. 7). In heating, the bubble usually disappeared first, then the inclusions burst at a temperature varying from 307.6 to 491.3 $^{\circ}\text{C}$ (Table 2).

3.2 Laser Raman spectroscopic analyses

The Raman results show that the liquid phase of the I-type fluid inclusions was H_2O , and the vapor phase (Fig. 8a, b) had mainly H_2O (3473.2 cm^{-1}) and a small amount of CO_2 ($1386.3, 1284 \text{ cm}^{-1}$). The vapor phase of IIa-type inclusions (Fig. 8c, d) contained mainly H_2O and CO_2 , with a small amount of CH_4 (2922.8 cm^{-1}) locally. The vapor

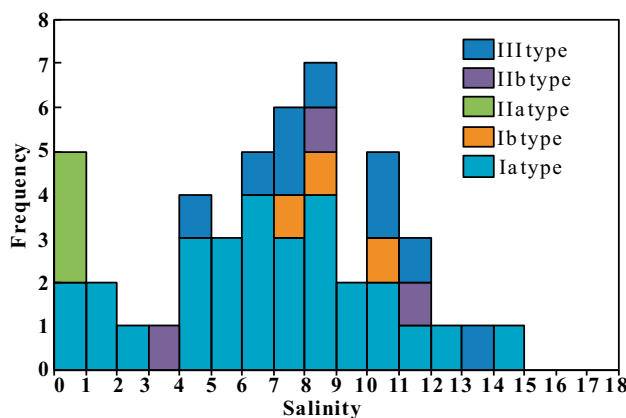


Fig. 7 Frequency histogram of salinities (wt% NaCl eq.)

phase of the IIb-type fluid inclusions (Fig. 8e) was mainly CO₂, with a small amount of CH₄ (2913 cm⁻¹) and N₂ (2328.2 cm⁻¹). In III-type multiphase inclusions (Fig. 8f), the cubical opaque daughter mineral was identified as pyrite (354 and 356 cm⁻¹). The round and triangular opaque mineral particles could be chalcopyrite, but the particles were too small to show the characteristic Raman spectra. In this study, calcite minerals (1087 cm⁻¹) were also identified in the multiphase inclusion (Fig. 8f).

3.3 Sulfur isotopes

Chalcopyrite is the main sulfide in the Badi copper deposit. δ³⁴S values of the chalcopyrite had a narrow range of 13.3‰ to 15.5‰. Sulfur isotope values of five chalcopyrite samples separated from quartz-sulfide type ore were

between 13.9‰ and 14.9‰, with an average of 13.92‰. Sulfur isotope values of five chalcopyrite samples separated from sericite-sulfide type ore were between 14.4‰ and 15.5‰, with an average of 13.92‰.

3.4 Oxygen and hydrogen isotopes

δD values of water in fluid inclusions ranged from -87‰ to -107‰; δ¹⁸O values of quartz were 14.4‰ to 15.3‰ (Table 3). According to the oxygen isotope fractionation equation of mineral–water systems— $1000\ln\alpha_{\text{quartz-water}} = 3.38 \times 10^6/T^2 - 3.40$ (Clayton et al. 1972)—and the formation temperatures inferred from homogenization temperatures of fluid inclusions, δ¹⁸O values of the ore-forming fluids were calculated to vary from 4.96‰ to 5.86‰.

4 Discussion

4.1 Characteristics of the ore-forming fluids

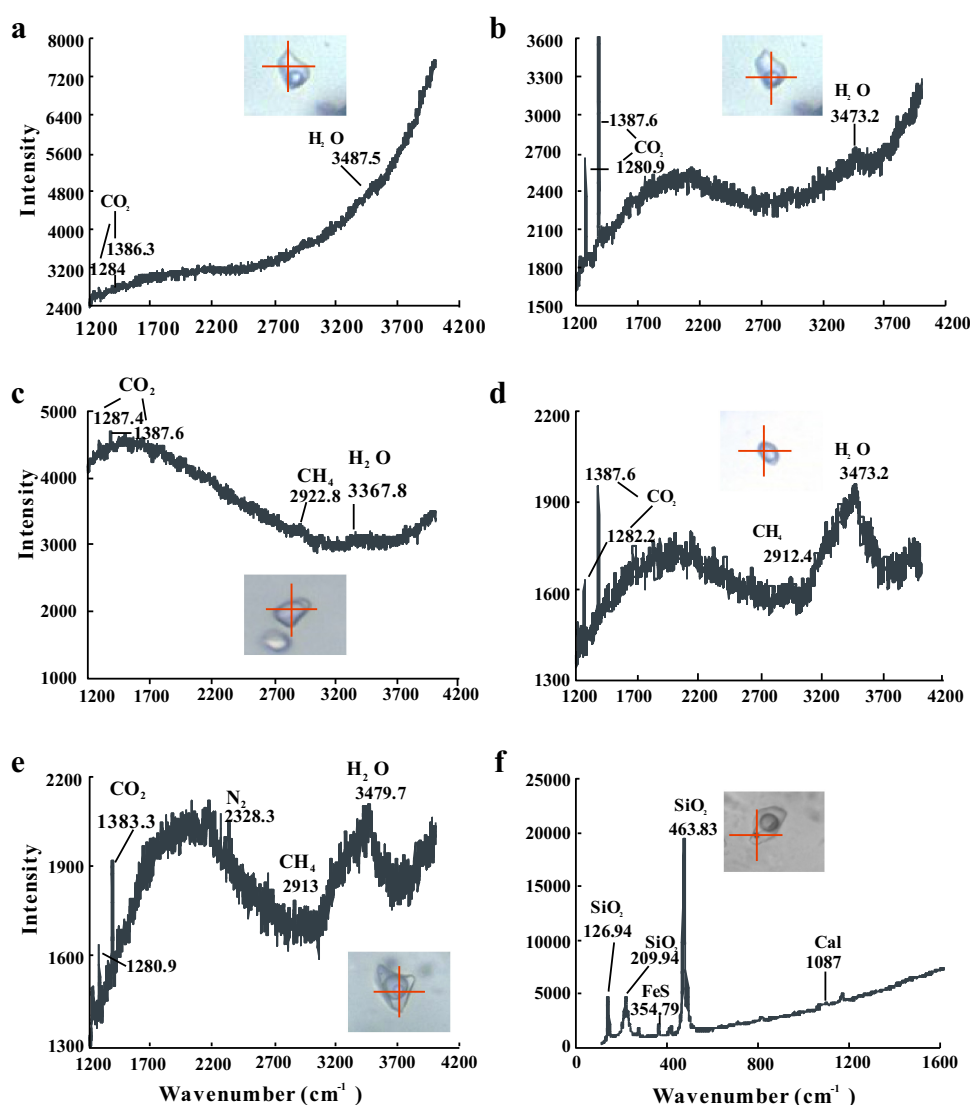
In this study, we obtained homogenization temperature and salinity data from 26 vapor–liquid two-phase fluid inclusions, 14 CO₂-bearing fluid inclusions (including three-phase and two-phase) and nine daughter mineral-bearing fluid inclusions. The ore-forming fluids of the Badi deposit plot in three different fields in the homogenization temperature (Th) versus salinity diagram (Fig. 9):

Table 2 Summary of microthermometric data on fluid inclusions of the Badi copper deposit

Sample	Type	T _{m,ice} (°C)	T _{m,clath} (°C)	T _{h,CO₂} (°C)	T _{h,total} (°C)	Salinity (wt% NaCl equiv)
LF001	IIb		5.9–8.4 (7)	22.6–30.4 (L) 25.8 (V)	193.4–296.3	3.15–7.54
	Ib	-4.8 (1)			230.2	7.59
	III	-7 to -2.8 (5)			380.3–458.7	4.55–10.48
LF002	III	-4.9 (1)			307.6	7.68
	Ia	-6.3 to -0.6 (6)			116.4–216.3	1.06–9.60
LF003	Ia	-10.7 to -1.2 (7)			163.1–186.2	2.07–14.67
	III	-9.7 (1)			491.3	13.62
LF004	Ia	-5.1 to -0.3 (6)			143.2–322	0.53–8.00
	Ib	-6.9 to -4.8 (2)			193–457	7.59–10.36
	III	-7.8 (1)			364.6	11.46
LF005	IIa		-0.4 to 5.1 (2)	16.6–21.6 (V)	211.7–269	0.53–0.71
	IIb		3–5.1 (3)	18.7 (V) 21.5–28.4 (L)	200.2–256.6	8.82–11.89
	III	-3.8 (1)			367.9	6.08
	Ia	-3.8 to -0.2 (4)			125.3–254.3	0.35–6.16

T_{m,ice}, temperature of final ice melting; T_{m,clath}, melting temperature of the CO₂ clathrate; T_{h,CO₂}, partial homogenization temperature of carbonic inclusion; T_{h,total}, homogenization temperatures and burst temperatures; all the number in the bracket is number of analysis data

Fig. 8 Raman spectra of fluid inclusions. **a** CO₂ and H₂O in the vapor phase of Ia type; **b** CO₂ and H₂O in the vapor phase of Ib type; **c, d** CO₂, H₂O and CH₄ in the vapor phase of IIa type; **e** CO₂, H₂O, CH₄, N₂ in the vapor phase of IIb type; **f** FeS and calcite daughter minerals from III type



- (1) H₂O–NaCl fluids. These were divided into two subtypes. Low temperature ore-forming fluid with homogenization temperatures concentrated from 150 to 220 °C and salinities from 0.35 wt% to 14.67 wt% NaCl equivalent. These data mainly concentrated in the C region of Fig. 9, a low-temperature, low to middle salinity fluid. Fluid with homogenization temperatures from 254 to 322 °C and salinities from 0.53 wt% to 8.00 wt% NaCl equivalent was defined as mid-temperature H₂O–NaCl fluid in this paper.
- (2) CO₂-bearing ore-forming fluids. These correspond to IIb-type and distributed in the B region of Fig. 9. Homogenization temperatures varied from 156.6 to 296.3 °C, and salinities from 3.15 wt% to 11.89 wt% NaCl equivalent.
- (3) Ore-forming fluids of high Fe content and high sulfur fugacity. This type of fluid inclusion had

homogenization temperatures of 307.6 to 491.3 °C, and salinities of 4.55 wt% to 13.62 wt% NaCl equivalent, distributed near the critical curve. The fluid inclusions contained daughter pyrite. In Fig. 9 these data mainly distributed in the A region.

4.2 Origin and depositional mechanism of the ore-forming materials

Chalcopyrite is most abundant sulfide in the Badi deposit. $\delta^{34}\text{S}$ values of the chalcopyrite were 13.3‰ to 15.5‰ (Table 3). This suggests an uniform sulfur source in the Badi deposit. The $\delta^{34}\text{S}$ of sulfide can represent the $\delta^{34}\Sigma\text{S}$ composition of the ore-forming fluid under the condition of low oxygen fugacity (Reed and Palandri 2006; Ohmoto 1972). The $\delta^{34}\Sigma\text{S}$ of hydrothermal fluids of the Badi deposit are approximately equal to the $\delta^{34}\text{S}$ values of

Table 3 Summary of sulfur isotope compositions of the Badi copper deposit

Sample	Mineral	Test Mineral	$\delta^{34}\text{S}_{\text{CDT}} (\text{\textperthousand})$
LB018	Chalcopyrite-bearing quartz veins	Chalcopyrite	13.9
LB020	Chalcopyrite-bearing quartz veins	Chalcopyrite	14.2
LB021	Chalcopyrite-bearing quartz veins	Chalcopyrite	14.3
LB023	Chalcopyrite-bearing quartz veins	Chalcopyrite	13.3
LF003	Chalcopyrite-bearing quartz veins	Chalcopyrite	13.9
DGB-1	Chalcopyrite veins	Chalcopyrite	14.6
DGB-2	Chalcopyrite veins	Chalcopyrite	14.4
DGB-3	Chalcopyrite veins	Chalcopyrite	14.4
DGB-4	Chalcopyrite veins	Chalcopyrite	14.6
DGB-5	Chalcopyrite veins	Chalcopyrite	15.5

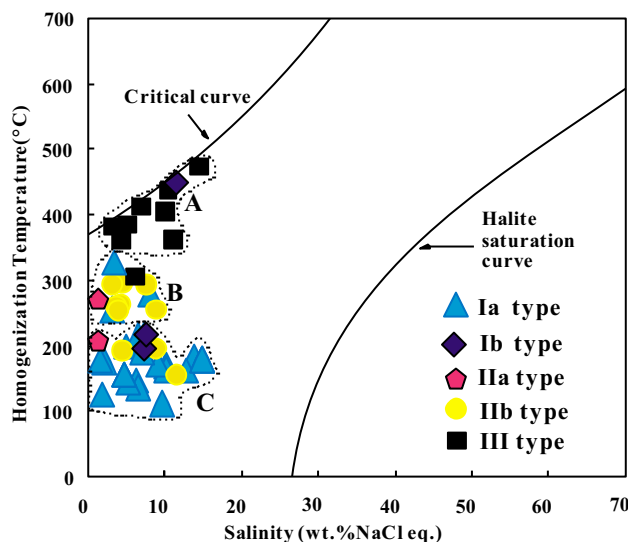


Fig. 9 Homogenization temperature (Th) versus salinity diagram for fluid inclusions (FIs) from the Badi copper deposit

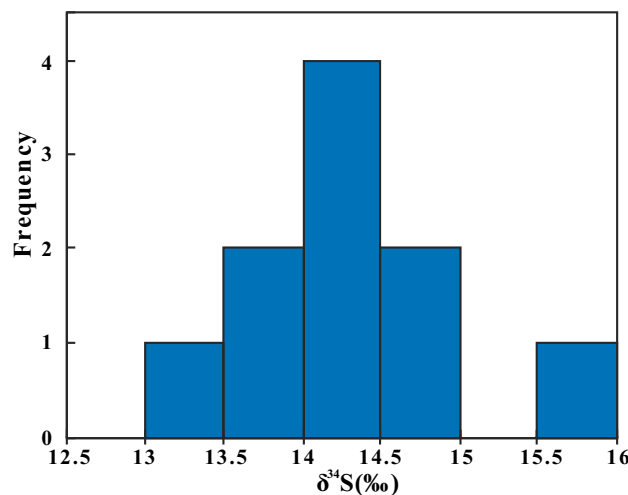


Fig. 10 Frequency histogram of $\delta^{34}\text{S}$ values for sulfide minerals from the Badi copper deposit

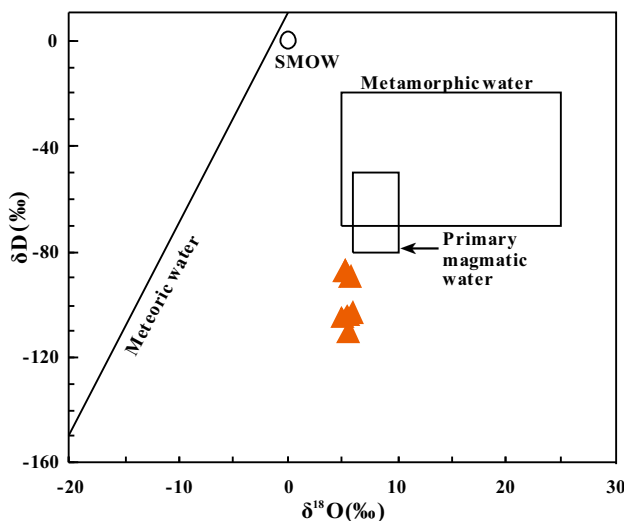
chalcopyrite (Fig. 10), a value consistent with the Proterozoic seawater sulfur isotope value (10‰ to 18‰, Strauss 1993), suggesting that sulfur in the Badi deposit is mainly from seawater. As shown in Table 2, the sulfur isotope values of chalcopyrite from quartz-sulfide type ore were 13.9‰ to 14.9‰, with an average of 13.92‰. Sulfur isotope values of chalcopyrite from sericite-sulfide type ore were 14.4‰ to 15.5‰, with an average of 14.70‰. Quartz-sulfide ore formed later than sericite-sulfide ore based on petrographic observation. Sulfur isotopic values from early to late display a decreasing trend that could be a result of the reservoir effect.

In Fig. 11, the O–H isotopic values of the ore-forming fluid plot mainly in the transition field of magmatic water. Therefore, we suggest that the fluid in the ore-forming stage of this deposit is mainly mixed water. δD values decreased from sample LB022 to LB018, while $\delta^{18}\text{O}$ values did not change much (Table 4). The reason for this may be a change in oxygen fugacity in the fluid; hydrogen isotope fractionation between water and reduced species, such as CH_4 or H_2 ; or the mixing of rainwater (Taylor 1974; Mi et al. 2017). The hydrogen isotope values were $-87\text{\textperthousand}$ to $-110\text{\textperthousand}$, with an average of $-98.6\text{\textperthousand}$ in quartz-sulfide type ore samples; oxygen isotope values were 4.95‰ to 5.56‰, with an average of 5.26‰. In sericite-sulfide type ore, hydrogen isotope values were $-89\text{\textperthousand}$ to $-103\text{\textperthousand}$, with an average of $-96\text{\textperthousand}$, and oxygen isotope value were 5.66‰ to 5.86‰, with an average of 5.76‰. Quartz samples separated from quartz-sulfide veins had lower hydrogen and oxygen isotope values than those separated from sericite-sulfide ore. This may be due to increasing input of meteoric water in the late ore-forming stage (Fig. 11).

Differences of vapor–liquid ratios were detected in I-type vapor–liquid two-phase inclusions. In the same homogenization temperature range, fluid inclusions with higher vapor–liquid volume ratios homogenized to vapor phase, while lower vapor–liquid ratios homogenized to liquid phase. Ia-type and Ib-type as well as III-type fluid

Table 4 Summary of oxygen and hydrogen isotope data of the Badi copper deposit

Sample	Mineral	Test mineral	Th (°C)	δD_{V-SMOW} (‰)	$\delta^{18}O_{V-SMOW}$ (‰)	$\delta^{18}O_{H_2O}$ (‰)
LB018	Chalcopyrite-bearing quartz veins	Quartz	346	– 105	14.4	4.96
LB019	Chalcopyrite-bearing quartz veins	Quartz	334	– 110	15	5.56
LB020	Chalcopyrite-bearing quartz veins	Quartz	334	– 104	14.8	5.36
LB021	Chalcopyrite-bearing quartz veins	Quartz	341	– 87	14.6	5.16
LB022	Chalcopyrite-bearing quartz veins	Quartz	341	– 87	14.7	5.26
LF003	Chalcopyrite-bearing quartz veins	Quartz	327	– 103	15.3	5.86
LG033-1	Chalcopyrite-bearing quartz veins	Quartz	331	– 89	15.1	5.66

**Fig. 11** δD_{H_2O} – $\delta^{18}O_{H_2O}$ plots of fluid inclusions at the Badi copper deposit

inclusions seem closely related in space, often appearing in the same field. Petrography and temperature data suggest fluid inclusions hosted in ore-bearing vein may have been captured in the boiling system (Bisehoff 1991; Zhang 1997; Qi et al. 2007; Zhang et al. 2004). During the fluid boiling process, escape of CO₂ and other volatiles can effectively reduce the temperature and increase the pH of ore-forming fluid (Li et al. 2007). On the other hand, it may form a super saturated fluid and trigger sulfide deposition (Chen et al. 2004, 2007).

5 Conclusions

(1) The Badi copper deposit contains four types of fluid inclusions in sulfide-bearing veins. They are vapor-liquid two-phase fluid inclusions with homogenization temperatures of 116.4 to 457.0 °C; CO₂-bearing two-phase fluid inclusions with homogenization

temperatures of 211.7 to 269 °C; CO₂-rich three-phase fluid inclusions with partial homogenization temperatures of 21.5 to 30.4 °C and final homogenization temperatures of 156.6 to 296.3 °C; and daughter mineral-bearing three-phase fluid inclusions with burst temperatures of 307.6 to 491 °C. The vapor phase of fluid inclusion samples from the Badi copper deposit mainly consisted of H₂O and CO₂, with small amounts of N₂ and CH₄; the main component of the liquid phase was H₂O.

(2) Isotope geochemistry results suggest that sulfur mainly derived from contemporaneous sea water, and the ore-forming fluids were a mixture between magmatic fluid and meteoric water. Deposition of sulfide minerals mainly resulted from fluid boiling.

Acknowledgements This research was jointly supported by the Geological Survey of China (Grant No. 1212011140050) and the National Natural Science Foundation of China (Grant No. 41663006). We are grateful to Prof. Yuzhao Hu and M. S Jie Su for assistance during the field investigations.

References

- Bisehoff J (1991) Densities of liquids and vapors in boiling NaCl–H₂O solutions: a PVTX summary from 300 to 500 C. Am J Sci 291:309–338
- Bodnar RJ (1989) Revised equation and table for determining the freezing point depression of H₂O–NaCl solutions. Geochim Cosmochim Acta 57:683–684
- Bodnar RJ (1993) Revised equation and table for determining the freezing point depression of H₂O–NaCl solutions. Geochim Cosmochim Acta 57:683–684
- Chen HY, Chen YJ, Ni P, Zhang ZJ (2004) Fluid inclusion study of the Sawayardun Au deposit in Southern Tianshan, China: implication for ore genesis and exploration. J Miner Petrol 24(3):46–54
- Chen YJ, Ni P, Fan HR, Pramjno F, Lai Y, Su WC, Zhang H (2007) Diagnostic fluid inclusion of different types hydrothermal gold deposits. Acta Petrol Sin 23(9):2085–2108
- Clayton RN, O’Neil JR, Mayeda TK (1972) Oxygen isotope exchange between quartz and water. J Geophys Res 77:3057–3067

- Collins PLF (1979) Gashydrate in CO₂-bearing fluid inclusions and the use of freezing data for estimation of salinity. *Econ Geol* 74:1435–1444
- Cui JH, Ren T, Hu YZ, Huang JG, Wang L, Yang JK, Su J (2014) A study on petrology and tectonic setting of upper member of Shigu group: a case of Badi region in Northwest Yunnan Province, China. *Acta Miner Sin* 34(2):199–207
- Davis DW, Lowenstein TK, Spencer RJ (1990) Melting behavior of fluid inclusions in laboratory-grown halite crystals in the systems NaCl–H₂O, NaCl–KCl–H₂O, NaCl–MgCl₂–H₂O, and NaCl–CaCl₂–H₂O. *Geochim Cosmochim Acta* 54:591–601
- Feng JR, Mao JW, Pei RF, Li C (2011) Ore-forming fluids and metallogenesis of Nanyangtian tungsten deposit in Laojunshan Southeastern Yunnan Province. *Miner Depos* 30(3):403–419
- Gou TZ, Zhong H, Leng CB, Wu KW (2010) Geochemistry of platinum-group elements of the Lannitang epithermal Cu–Au deposit in the Zhongdian region, Yunnan Province, SW China. *Acta Miner Sin* 30(3):319–323
- Hu B, Dai TG, Hu RZ, Guo Q (2005) Division of crustobody tectonic units and their evolution-movement characteristics in Western Yunnan Province. *Geotecton Metall* 29(4):537–544
- Jin CH, Fan WY, Zhang Y, Zhang H, Shen ZW, Gao JH (2013) Trace element composition and U–Pb chronology of zircons in monzonite porphyry from the Langdu copper deposit in Zhongdian and their geological significance. *Geotecton Metall* 37(2):262–272
- Leng CB, Zhang XC, Hu RZ, Wang SX, Zhong H, Wang WQ, Bi XW (2012) Zircon U–Pb and molybdenite Re–Os geochronology and Sr–Nd–Pb–Hf isotopic constraints on the genesis of the Xuejiping porphyry copper deposit in Zhongdian, Northwest Yunnan, China. *J Asian Earth Sci* 60(22):31–48
- Li KQ (2003) The metamorphism, deformation and stratigraphic division of Shigu schist in Northwest Yunnan. *Yunnan Geol* 22(3):329–335
- Li WB, Lai Y, Sun XW, Wang BG (2007) Fluid inclusion study of the Bainaimiao Gu–Au deposit in Mongolia, China. *Acta Pet Sin* 23(9):2165–2176
- Li WC, Zeng PS, Hou ZQ, White NC (2011) The Pulang porphyry copper deposit and associated felsic intrusions in Yunnan Province, Southwest China. *Econ Geol* 106(1):79–92
- Li WC, Wang KY, Yin GH, Qin DH, Yu HJ, Xue SR, Wan D (2013) Geochemical characteristics of ore-forming fluids and genesis of Hongshan copper deposit in Northwestern Yunnan Province. *Acta Pet Sin* 29(1):270–282
- Liu HC (1983) The distribution and genesis of metallic ore deposits in Yunnan Province. *Miner Depos* 2(4):19–25
- Liu B, Shen K (1999) Fluid inclusion thermodynamics. Geological Publishing House, Beijing, pp 1–290
- Liu HB, Jin GS, Li JJ, Han J, Zhang JF, Zhang J, Zhong FW, Guo DQ (2013) Determination of stable isotope composition in uranium geological samples. *World Nucl Geosci* 30(30):174–179
- Liu XL, Li WC, Hang N (2016) Zircon U–Pb age and geochemical characteristics of the quartz monzonite porphyry from the Zhuoma deposit Yunnan, China. *Bull Miner Pet Geochem* 35(1):109–117
- Lu HZ, Fan HR, Ni P, Ou GX, Shen K, Zhang WH (2004) Fluid inclusions. Science Press, Beijing, pp 132–208
- Mi KF, Liu ZJ, Li CF, Liu RB, Wang JP, Peng RM (2017) Origin of the Badaguan porphyry Cu–Mo deposit, Inner Mongolia, Northeast China: constraints from geology, isotope geochemistry and geochronology. *Ore Geol Rev* 81:141–172
- Ohmoto H (1972) Systematics of sulfur and carbon isotopes in hydrothermal ore deposits. *Econ Geol* 67(5):551–578
- Pan JY, Zhang Q, Ma DS, Li CY (2000) Stable isotope geochemical characteristics of the Yangla copper deposit in Western Yunnan Province. *Acta Miner Sin* 20(4):44–49
- Qi JP, Cheng YJ, Ni P, Lai Y, Ding JY, Song YW, Tang GJ (2007) Fluid inclusion constraining on the origin of the lingshuibeigou Pb–Zn–Ag deposit Henan Province. *Acta Pet Sin* 23(9):2119–2130
- Reed MH, Palandri J (2006) Sulfide mineral precipitation from hydrothermal fluids. *Rev Miner Geochem* 61:609–631
- Ren JS (1980) Geotectonic evolution of China. Science Press, Beijing, pp 1–140
- Shao SL (1989) The general characteristics of shigu metamorphic belt in Western Yunnan Province. *Acta Pet Sin* 2(1):78–83
- Strauss H (1993) The sulfur isotopic record of Precambrian sulfates, new data and a critical evaluation of the existing record. *Precambrian Res* 63:225–246
- Tang JX, Zhang L, Li ZJ, Chen JP, Huang W, Wang Q (2006) Porphyry copper deposit controlled by structural nose trap: yulong porphyry copper deposit in eastern Tibet. *Miner Depos* 25(6):652–662
- Taylor HP (1974) The application of oxygen and hydrogen isotope studies to problems of hydrothermal alteration and ore deposition. *Econ Geol* 69:843–883
- Wang AJ, Cao DH, Guan Y, Liu JL, Li WC (2009) Metallogenic belts of southern three rivers region, southwest China: distribution, characteristics and discussion. *Acta Geol Sin* 83(10):1365–1375
- Xu LL, Bi XW, Hu RZ, Zhang XC, Su WC, Qu WJ, Hu ZC, Tang YY (2012) Relationships between porphyry Cu–Mo mineralization in the Jinshajiang–Red River metallogenic belt and tectonic activity: constraints from zircon U–Pb and molybdenite Re–Os geochronology. *Ore Geol Rev* 48(1–2):460–473
- Xu LL, Bi XW, Hu RZ, Qi YQ, Tang YY, Wang XS, Zhu JJ (2015) Redox states and genesis of magmas associated with intra-continental porphyry Cu–Au mineralization within the Jinshajiang–Red River alkaline igneous belt, SW China. *Ore Geol Rev* 73:330–345
- Zhai MG, Cong BL (1993) The diancangshan–shigu metamorphic belt in Yunnan, China: their geochemical and geochronological characteristics and division of metamorphic domains. *Acta Pet Sin* 9(3):227–239
- Zhai MG, Cong BL, Qiao GS, Zhang RY (1990) Sm–Nd and Rb–Sr geochronology of metamorphic rocks from SW Yunnan orogenic zones, China. *Acta Pet Sin* 16(4):1–11
- Zhang DH (1997) Some new advances in ore-forming fluid geochemistry on boiling and mixing of fluids during the processes of hydrothermal deposits. *Adv Earth Sci* 12(6):546–552
- Zhang J, Chen YJ, Li GP, Li ZL, Wang ZG (2004) Characteristics of ore geology and fluid inclusion of the Yindonggou silver deposit, Neixiang County, Henan Province: implication for metallogenic type. *J Mineral Petrol* 24(3):55–64
- Zu B, Xue C, Zhao Y, Qu WJ, Li C, Symons DTA, Du AD (2015) Late cretaceous metallogeny in the Zhongdian area: constraints from Re–Os dating of molybdenite and pyrrhotite from the Hongshan Cu deposit, Yunnan, China. *Ore Geol Rev* 64(1):1–12